Sensors & Actuators: A. Physical 409 (2026) 118047

Contents lists available at ScienceDirect

Sensors and Actuators: A. Physical

journal homepage: www.journals.elsevier.com/sensors-and-actuators-a-physical

Pivot-stable electrostatic rotary MEMS structure for alignment-critical applications

Navid Heidari*, Julian L. Pita Ruiz, Mathieu Gratuze, Seyedfakhreddin Nabavi, Michaël Ménard, Frederic Nabki

LaCIME, Department of Electrical Engineering, École De Technologie Supérieure, 1100 Notre-Dame Street West, Montréal, H3C 1K3, Québec, Canada

HIGHLIGHTS

- Introduces a pivot-stable electrostatic rotary MEMS actuator optimized for alignment-critical MOEMS applications.
- Employs curved comb-drive electrodes with symmetric U-shaped suspension springs to enable controlled bidirectional in-plane rotation with a stable center of rotation.
- Achieves ±2.2° angular displacement at 150 V, with close agreement between analytical modeling, FEM simulations, and experimental measurements.
- Demonstrates exceptionally low parasitic motion (X/Y < 190 nm, Z < 300 nm), which is explicitly quantified and shown to preserve alignment during rotation.
- Optical FDTD simulations confirm robust optical performance, showing <1% variation in coupling efficiency across the full actuation range, supported by an integrated electrostatic gap-closing mechanism for reduced insertion loss.

ARTICLE INFO

Keywords:
MEMS
Rotary actuator
Electrostatic actuation
Micro-fabrication
MOEMS

ABSTRACT

This work presents a novel electrostatically actuated rotary MEMS structure optimized for high-precision in-plane rotation with low parasitic displacement. The design integrates curved comb-drive electrodes with symmetrical U-shaped suspension springs to enable controlled bidirectional rotation while minimizing undesirable lateral and out-of-plane motion. Analytical modeling, finite element simulations, and experimental measurements consistently demonstrate a maximum angular displacement of ±2.2° at 150 V, with unwanted lateral translational motion confined below 190 nm along both the X and Y directions, and out-of-plane motion confined under 300 nm in the Z direction. The platform stable center of rotation and suppressed parasitic displacement make it highly suitable for applications such as MOEMS-based optical switches, where alignment precision is critical. In addition, the platform features a lateral gap-closing mechanism actuated electrostatically, enabling tunable displacement for alignment-critical optical applications while preventing pull-in through stopper integration. Furthermore, this work provides an analytical formulation of torque and stiffness. The proposed device occupies an area of 1 mm × 2 mm and is fabricated using the PiezoMUMPs process with a 10 μm thick device layer.

1. Introduction

Micro-electro-mechanical-systems (MEMS) have significantly impacted modern technology by integrating mechanical and electrical components at the microscale. These devices, fabricated using semiconductor processes, enable precise sensing and actuation in compact and efficient form-factors. Their applications span across industries, from automotive safety systems with MEMS accelerometers for airbag deployment [15,20,37], aerospace [6,19], to biomedical devices incorporating lab-on-a-chip diagnostics and implantable pressure sensors [16,24,25,35,47]. An important feature of MEMS devices is their integration capability with optical components for telecommunications, particularly in data centers, where they are used to steer light carrying data between optical channels [44]. The versatility and scalability of MEMS technology continue to drive innovation across both consumer and specialized applications [38].

MEMS devices can feature different actuation mechanisms, each with advantages and limitations, which determine their motion and functionality. Electromagnetic actuators can generate large displacements with

* Corresponding author.
Email address: navid.heidari.1@ens.etsmtl.ca (N. Heidari).

https://doi.org/10.1016/j.sna.2026.118047
Received 27 December 2025; Received in revised form 1 May 2026; Accepted 25 May 2026
Available online 2 June 2026
0924-4247/© 2026 The Author(s). Published by Elsevier B.V. This is an open access article under the CC BY license (http://creativecommons.org/licenses/by/4.0/).

low voltage but pose fabrication challenges due to the integration of coils and magnetic materials and require large areas [29,48]. Piezoelectric actuators offer high-speed and precise motion but require high electric fields and introduce process complexities when integrating piezoelectric films [4,11,36]. Thermal actuators, which rely on resistive heating, produce large forces and displacements at low input voltages, but their response time is limited by heating and cooling cycles, and they have relatively high power consumption [8,18,43,53]. In contrast, electrostatic actuators, despite requiring high operating voltages and exhibiting limited displacement due to pull-in instability, are commonly favored in MEMS devices for their low power consumption and compatibility with standard semiconductor fabrication processes [27,34].

Among electrostatic actuation configurations, comb-drive actuators have gained prominence due to their efficiency and scalability [12,33,45,49]. These actuators consist of interdigitated fingers, with one set fixed to the substrate and the other attached to a movable structure through a set of compliant springs. When a voltage is applied, electrostatic forces pull the movable fingers toward the fixed ones, generating displacement [22]. Comb drives can generate higher forces by increasing the number of fingers or reducing the inter-finger gap, making them highly effective for various MEMS applications.

Conventional comb drives primarily facilitate linear motion [21]; however, in various applications rotational movement is desirable, such as in micro grippers [9,28], and optical switches [7,14,41]. Therefore, by constructing comb-drive electrodes in a circular or radial geometry, rotational motion can be achieved [14,41].

The ability to achieve rotational motion at the microscale has enabled a wide range of advanced applications. For example, MEMS-based rotary actuators are employed in laser beam scanning and positioning systems [2,3,17]. Huda et al. [17] proposed a rotary MEMS comb-drive actuator featuring a 2 mm movable arm developed for photonic applications. The actuator demonstrated a maximum angular deflection of 2.8° under a 100 V bias. Fabricated using SOI wafers and optimized deep reactive ion etching (DRIE), the device exhibits smooth sidewalls suitable for integration with optical systems, such as external cavity lasers and hybrid photonic platforms.

Rotary MEMS devices also find applications in RF systems. Kashani et al. [23] introduced a compact, electrostatically actuated rotary RF MEMS switch designed for antenna switching, operating at an actuation voltage of 50 V. Inertial sensors, including MEMS gyroscopes [13,51], utilize rotary actuation to sustain oscillation, thereby enabling high-precision angular rate measurements for navigation and motion tracking.

In biomedical systems, rotary MEMS structures facilitate precise control of optical components in endoscopic imaging [30,40]. Additionally, in micro-robotics, rotary MEMS actuators are leveraged for controlled movement in micromanipulation tasks, allowing for accurate operation in confined or delicate environments where conventional actuators are unsuitable [26].

Despite recent advancements, most rotary MEMS designs still struggle to fully mitigate unwanted motion during rotation. In high-precision applications such as optical switches, image scanners, and laser positioning systems, structural misalignment caused by lateral translational displacement can significantly degrade performance [1]. Even slight misalignment between the input and output waveguides in optical switches has been shown to increase insertion loss [14]. Therefore, it is essential to constrain the suspended structure to purely rotational motion, minimizing translational drift and other unintended displacements.

Accordingly in this work, a rotary MEMS structure is designed with U-shaped springs that function as mechanical hinges. These springs allow the structure to rotate while keeping it stable and preventing unwanted movements, making it more accurate for optical and other high-precision uses. The structure also includes an electrostatically actuated lateral gap-closing mechanism, designed to improve insertion loss in applications where coupling between input and output waveguides is critical, such as optical switches.

The remaining of this paper is organized as follows: Section 2 presents the proposed design, analytical modeling, and micro-fabrication process. Section 3 details the simulation and experimental results. In Section 4, the findings are discussed, and the performance of the proposed rotary MEMS actuator is compared with the state-of-the-art. Finally, Section 5 concludes the paper and highlights directions for future work.

2. Design, analytical model, and micro-fabrication process

2.1. Design

The MEMS device presented in this work is an electrostatically actuated structure devised to achieve rotational motion with minimal lateral displacement. Fig. 1(a) and (b) show the fabricated device, illustrating the top view and the most critical components of the structure, respectively. As can be seen in this figure, the proposed MEMS device has a symmetrical configuration, consisting of comb fingers on each side and a platform connected to U-shaped springs. The U-shaped springs are 4 μm wide and 10 μm thick. The entire structure, including the fingers and the platform, is supported by the beams of the U-shaped springs with dimensions $L_1 = L_2 = 180$ μm, $L_3 = 200$ μm, and $L_4 = 25$ μm. These attached beams provide the necessary mechanical stability while allowing the platform to rotate clockwise and counterclockwise freely. The ends of the two L_1 beams are the only points through which the suspended structure is anchored. To further clarify the mechanical behavior of the U-shaped flexure, a simplified schematic is presented in Fig. 2. The U-shaped beams act as compliant elements that enable rotational motion of the suspended platform through distributed bending along their segments. Under electrostatic actuation, the deformation is primarily accommodated by flexural bending of the beam sections, allowing the platform to rotate about its geometric center while maintaining structural symmetry. This configuration effectively suppresses parasitic translational motion and enhances rotational stability. Arrows in Fig. 2 indicate the qualitative direction of motion and bending at selected locations along the flexure.

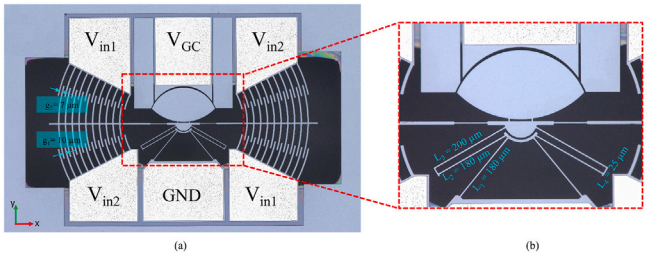


Fig. 1. Fabricated rotary MEMS structure: a) top view, b) zoomed view of the U-shaped spring.

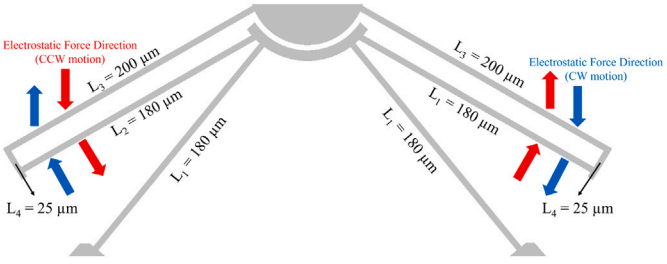


Fig. 2. Simplified schematic of the U-shaped flexure, illustrating the qualitative motion and bending directions under clockwise (CW, blue arrows) and counterclockwise (CCW, red arrows) electrostatic actuation (For interpretation of the references to color in this figure legend, the reader is referred to the web version of this article.).

Table 1
Dimensions of the device.

Geometry	Dimension [μm]
Finger Width	10
Platform Gap	7
Stopper Gap	3
L_1	180
L_2	180
L_3	200
L_4	25
Springs Width	4

Central to the device is an oval-shaped platform, which can be used to integrate RF or optical waveguides to control wave propagation on the structure. In optical switching applications, for example, this platform can be coated with silicon dioxide and silicon nitride (SiN) to function as a planar waveguide. Additionally, as proposed by Briere et al. [7], coating the back facet of the platform with metal enables it to act as a mirror, further expanding its optical manipulation capabilities.

Alongside the central platform are interdigitated comb structures, which are utilized for actuation. The fingers located on either side of the platform are free to move, while the fingers attached to the V_{in1} and V_{in2} electrodes remain fixed. When a voltage is applied between these electrodes and ground (GND), an electrostatic force is generated. The gaps between the fingers are intentionally made unequal ($g_1 \neq g_2$) to assist the U-shaped springs in suppressing undesirable lateral translational motion, as shown in Fig. 1. The curved geometry of the comb fingers causes the electrostatic force to act tangentially at a radial distance from the center of rotation, thereby generating a torque, while the U-shaped springs act as compliant flexural hinges that allow the resulting rotational motion of the movable fingers.

Both the stationary and movable fingers, along with the central platform, have the same circular center, each with a distinct radius. The common central origin enhances the structural stability and significantly reduces any unwanted lateral translational movement of the platform during rotation. The detailed physical dimensions of the proposed MEMS structure are provided in Table 1.

The bi-directional rotational motion of the device is achieved by applying voltage to specific electrodes. Applying voltage to the V_{in1} electrode induces a counterclockwise (CCW) motion, whereas applying voltage to the V_{in2} electrode results in a clockwise (CW) motion.

To allow the platform to rotate freely, a gap must be maintained between the platform and the V_{GC} electrode. However, in applications such as optical switches, it is important to minimize this gap once the waveguides are aligned in order to reduce insertion loss for both the input and output light [14]. When a voltage is applied to the V_{GC} electrode, the gap decreases due to electrostatic attraction, as illustrated in Fig. 1(b). This gap-closing mechanism has been previously explored in earlier work on optical MEMS switch applications [14].

The gap-closing function in the proposed design can be activated under two different operating conditions. In the first case, the platform remains at rest without any rotational actuation (i.e., at 0 V on the comb drives), and the V_{GC} electrode is used to pull the platform closer to the fixed surface. This is particularly useful in cases where optical waveguides are placed on the V_{GC} electrode, as presented in [14]. In the second scenario, the platform is first rotated to a desired angle by applying a voltage to the curved comb fingers (CW or CCW), and then a voltage can be applied to the V_{GC} electrode to close the gap. Importantly, the gap-closing mechanism does not interfere with the achieved rotation angle such that it simply reduces the spacing between the platform and the fixed surface to minimize optical insertion loss of potential waveguides present on the structure.

During the process of translational electrostatic actuation to close this gap, the electrodes gradually approach each other until they reach a critical distance, causing them to collapse and short circuit, a phenomenon known as pull-in. This pull-in can be calculated with the following equation [22]:

$$V_{pi} = \sqrt{\frac{8}{27}\frac{kg^3}{\varepsilon A}}, \tag{1}$$

where k denotes stiffness, g is the initial gap between the platform and the electrode, ε is the permittivity, and A is the common electrode area. To prevent direct electrode contact when pull-in occurs, a set of stoppers has been placed on both sides of the platform, as can be seen in Fig. 1(b). The gap between the platform and the electrode is 5 μm, and the gap from the stoppers to the platform is 3 μm. This prevents contact with the V_{GC} electrode when the gap is closed, maintaining the device structurally safe.

2.2. Analytical model

The interaction between the electrostatic forces within the comb drive structure generates a torque, ultimately resulting in angular displacement. The torque, denoted as τ can be determined using [42]:

$$\tau = F_{es} \times R, \tag{2}$$

where R represents the radial distance from the center to the fingers, and F_{es} corresponds to the electrostatic force acting on the system. To calculate the overall torque produced by the curved comb fingers, the analytical model proposed by Tu et al. [42] is used, in which the curved comb drives are approximated as parallel plate electrodes, and the fringing field effects are neglected.

The torque generated by electrostatic forces is influenced by two capacitances, C_g, which accounts for the capacitance between the movable and fixed fingers, and C_f, which corresponds to the capacitance formed at the tip of the movable fingers and the sidewalls of the fixed fingers. Since both capacitances contribute distinct torques (τ_f from C_g and τ_g from C_f), the total torque is given as:

$$\tau_{\text{total}} = \tau_f + \tau_g. \tag{3}$$

The torque expressions in Eqs. (4) and (5) are derived by integrating the electrostatic force along the curved comb fingers with respect to the radial distance from the center of rotation. A similar approach has been widely used in the modeling of electrostatic comb-drive actuators, where the force is first obtained from the partial derivative of the stored electrostatic energy (i.e., capacitance variation) and then converted into torque based on the effective moment arm. Using the parameters defined in Table 1 and the structural illustration in Fig. 1, the individual torques can be expressed mathematically as follows Tu et al. [42].

$$\tau_g = \frac{1}{2}\varepsilon_0 \cdot t \cdot V_{\text{in}}^2 \cdot \sum_{i=1}^{n-1}\left[\left(\ln\left(\frac{R_0 + 2i\cdot(W_f+g)}{R_0 + 2i\cdot(W_f+g) - g}\right)\right)^{-1} + \left(\ln\left(\frac{R_0 + (2i+1)\cdot(W_f+g)}{R_0 + 2i\cdot(W_f+g) + W_f}\right)\right)^{-1}\right] \tag{4}$$

and

$$\tau_f = \frac{1}{2}\varepsilon_0 \cdot W_f \cdot V_{\text{in}}^2 \cdot \frac{1}{\left(\frac{1}{2}\theta_r - \theta_0 - \theta\right)^2} \cdot \sum_{i=0}^{n-1}\left(\frac{1}{R_0 + 2i\cdot(W_f+g)} + \frac{1}{R_0 + 2(i+1)\cdot(W_f+g)}\right) \tag{5}$$

Since in the proposed design the inter finger gaps are not uniform, τ_g must be computed separately for different gap values. Consequently, in (4), g should be replaced with both g_1 = 10 μm and g_2 = 7 μm to account for the variation. The torque applied to the structure also acts on the U-shaped suspension springs, inducing rotation of the central

platform. The resulting rotation can be characterized by the angular displacement θ, which quantifies the relative motion between the movable and fixed fingers. This angular displacement is explicitly considered in (5), where the input parameters include all the structural dimensions from Table 1. The primary variables influencing the system dynamics are the actuation voltage V_{in}, the number of comb fingers n, and the rotational angle θ. In the analytical model, idealized boundary conditions are assumed and fringing field effects are neglected to simplify its formulation. This approximation is reasonable for the present design, as the overlap between comb fingers dominates the electrostatic interaction. While neglecting fringing fields actually underestimates the total electrostatic force, the assumption of ideal, perfectly compliant boundary conditions overestimates the mechanical flexibility of the structure. The interplay of these simplifications is reflected in the discrepancy observed between the analytical, FEM, and experimental results.

The spring constant of the beams in the MEMS structure can have both torsional (k_θ) and linear components (k_x). The decision as to which stiffness is used depends on the type of the force acting on the structure. As shown in Fig. 1, the beam segments forming the U-shaped flexure are mechanically connected in series along the deformation path. This means that the applied electrostatic force is transmitted progressively through each segment, and the overall displacement of the platform is the sum of their individual structural deflections. This behavior is consistent with folded and serpentine flexure springs commonly used in MEMS devices. Consequently, the total spring constant for these series springs is calculated using the inverse sum of the individual beam stiffnesses [22]:

$$\frac{1}{k_{\text{total}}} = \frac{1}{k_{L1}} + \frac{1}{k_{L2}} + \frac{1}{k_{L3}} + \frac{1}{k_{L4}} \tag{6}$$

Considering that all the beams of the U-shaped spring are anchored at L_1, the remaining segments are suspended and free to move. Therefore, they can be modeled as cantilever beams with a stiffness given by Kaajakari [22].

$$k_x = \frac{3EI}{L^3} \quad , \quad k_\theta = \frac{GJ}{L} \tag{7}$$

$$I = \frac{wt^3}{12} \quad , \quad J = \frac{wt^3}{3}, \tag{8}$$

where E and G represent the Young's modulus and shear modulus of silicon, respectively, while I and J denote the second moments of area associated with the flexural and torsional stiffness of the beams. Based on these parameters, the total linear (k_{xt}) and torsional ($k_{\theta t}$) spring constants of the MEMS structure can be expressed as:

$$k_{xt} = \frac{Ewt^3}{4(2L_1^3 + L_3^3 + L_4^3)}, \tag{9}$$

$$k_{\theta t} = \frac{Gwt^3}{3(2L_1 + L_3 + L_4)}. \tag{10}$$

The linear spring constant predominantly governs the platform's gap-closing motion when an actuation voltage is applied to the V_{GC} electrode, whereas the torsional stiffness is the dominant factor during rotational actuation. This distinction arises from the direction of the applied electrostatic forces and the anchoring configuration of the suspension beams. When a voltage is applied to the V_{GC} electrode, the resulting electrostatic force pulls the central platform laterally along the Y-axis toward the stopper, reducing the gap. This translational motion is resisted by the linear stiffness k_x of the U-shaped beams. Conversely, applying an actuation voltage to the curved comb fingers generates a tangential electrostatic force along the comb arc, producing a torque that induces rotation about the central axis. This rotational motion is primarily opposed by the torsional stiffness k_θ. Since the entire movable structure, including the central platform and comb fingers, is anchored to the fixed substrate exclusively at the outer ends of the two symmetrically arranged L_1 beams (as shown in Fig. 1(b), the suspension system is designed to favor rotational compliance with minimal translational displacement. As a result, the torsional spring constant dominates during rotational actuation, whereas the linear spring constant governs the gap-closing behavior [5,31]. The resulting angular displacement can be estimated using the expression from Kaajakari [22], which shows it to be inversely proportional to the torsional stiffness k_θ such that

$$\theta = \frac{\tau_{\text{total}}}{k_{\theta t}}, \tag{11}$$

where τ_{total} can be obtained by (3). Using (3), (10) and (11), the angular displacement for a specific actuation voltage can be calculated. Fig. 3 shows the calculated value of the angular displacement up to 150 V, which is the pull-in voltage according to (1) (Table 2).

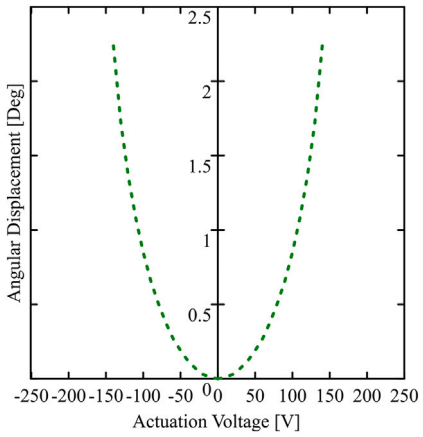


Fig. 3. Plot of the calculated angular displacement versus actuation voltage.

Table 2
Characteristics of the PiezoMUMPs process layers.

Layer	Thickness [μm]	Variability [μm]	Density [kg m^{-3}]	Layer name
Substrate	400	±5	2320	TRENCH
Silicon	10	±1	2320	SOI
Aluminum	1	±0.05	2700	PADMETAL

2.3. Micro-fabrication process

The MEMS structure was fabricated using the PiezoMUMPs process [10]. Fig. 4 presents both the fabricated device and schematic illustrations of its structure for better understanding of the design and layer composition. Fig. 4(a) provides an isometric view of the fabricated device captured using a scanning electron microscope (SEM, SU8230 Hitachi), clearly showing the fine features of the comb fingers and electrodes. All layers and a cross-sectional view of the fabricated MEMS structure are presented in Fig. 4(b) and (c). Although this process is typically used for piezoelectric devices, in this work, the piezoelectric layer was not used. Thus, only the structural silicon, oxide, and metal layers were used. The fabrication began with a silicon-on-insulator (SOI) wafer, which consists of a 10 μm-thick single-crystal silicon device layer with a (100) orientation, a 1 μm-thick buried oxide (BOX) layer, and a 400 μm-thick silicon substrate.

A 1 μm-thick aluminum layer was deposited and patterned using a liftoff process to form the contact pads for electrical connections. This step was performed prior to etching the silicon device layer to ensure proper alignment and coverage. After defining the structure using lithography, the silicon device layer was etched using DRIE to create the suspended mechanical structure.

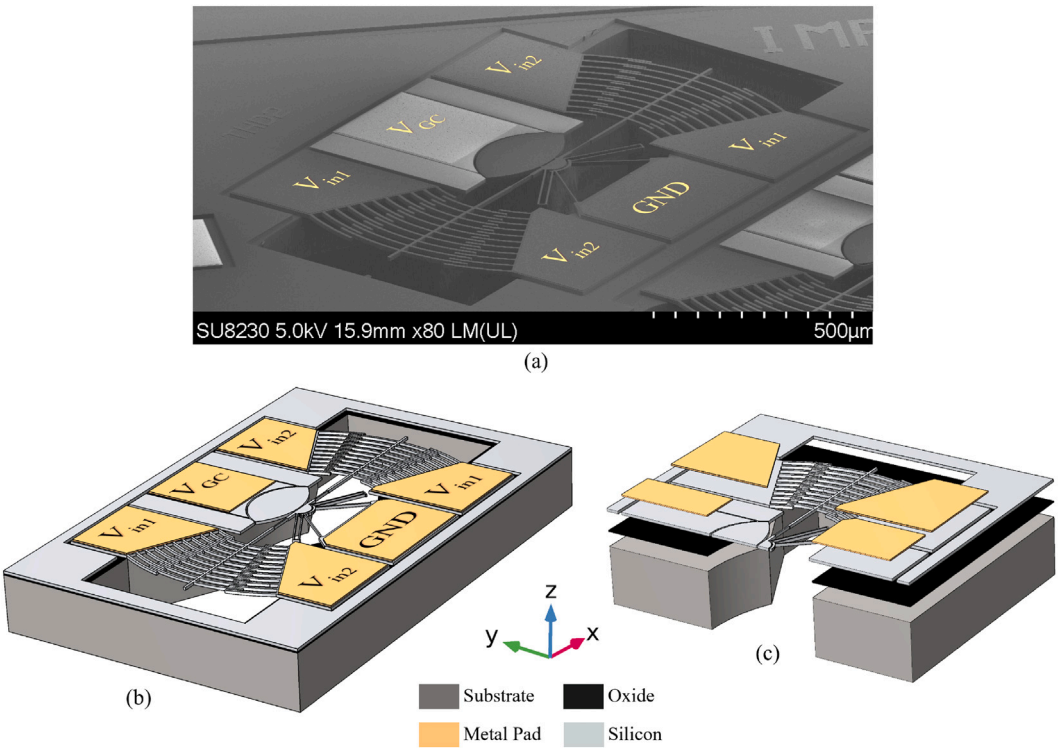


Fig. 4. Fabricated MEMS device: (a) isometric view captured using SEM, (b) 3D view of the layers, and (c) cross Section.

3. Results

3.1. Simulations

To analyze the behavior of the MEMS structure, a finite element method (FEM) simulation was conducted using the COMSOL (version 1.6) software suite. This analysis aims to determine the angular and gap-closing displacements as a function of actuation voltage. As detailed in Section 2.1, applying an actuation voltage to each pair of electrodes can result in either clockwise (CW) or counterclockwise (CCW) angular displacements. Fig. 5 shows the angular displacement of the fingers and the suspended platform. According to the simulations, the structure can withstand a maximum actuation voltage of 150 V before pull-in occurs at 160 V, leading to an angular displacement of 2.2° in both directions.

The most significant feature of the proposed design is its stable center of rotation, positioned at the geometric center of the structure. This stability is critical for alignment-sensitive applications, such as MOEMS optical switches. In these devices, parasitic translational motion during rotation would cause severe misalignment between optical waveguides and induce high insertion loss. Mechanically, this stability arises from the combined effect of the symmetric structural layout, the common geometric center of the curved comb fingers, and the compliant behavior of the U-shaped suspension springs, which together ensure that the generated electrostatic forces produce a balanced torque and constrain the motion about a fixed rotational point. Fig. 6(a) shows the center of rotation, while Fig. 6(b) presents a magnified view of this region, highlighting the possible directions of motion. The simulated displacement components in the X, Y, and Z directions presented in Fig. 6(c) are extracted precisely at this center of rotation. The structure can move in-plane along the X and Y axes, and out-of-plane along the Z-axis, which is perpendicular to the image plane. Fig. 6(c) presents the simulated translational displacements along the three axes of motion, where the Y-axis of the plot is the displacement in nanometers, the lower X-axis is the actuation voltage, and the upper X-axis corresponds to the angular displacement achieved in degrees.

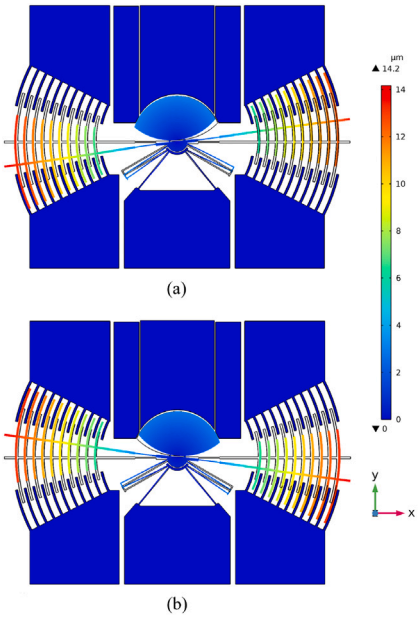


Fig. 5. FEM simulation of the angular displacement of the MEMS structure at an actuation voltage of 150 V: a) CW motion, b) CCW motion.

As the platform rotates CW, the simulations predict that the center of rotation shifts approximately 8 nm in the Y direction, 52 nm in the X direction, and 118 nm in the Z direction at 150 V, before pull-in. The same displacement occurs for CCW rotations but in opposite directions. In either case, the angular displacement reaches a maximum of 2.2° at 150 V.

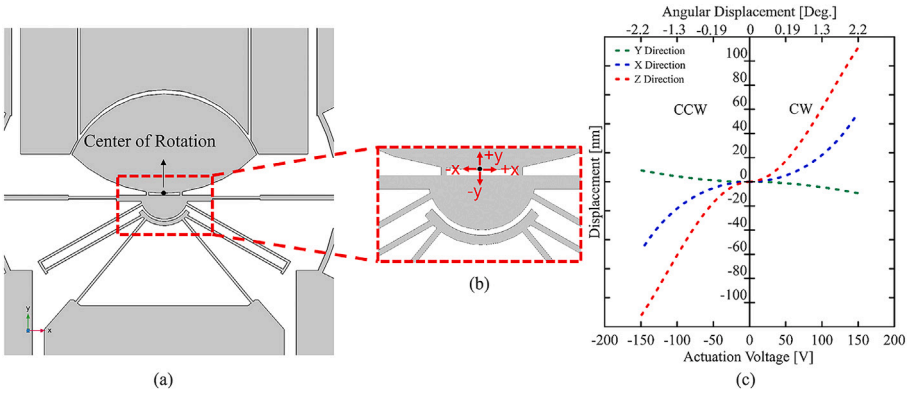


Fig. 6. A) MEMS structure showing the center of rotation, b) Magnified view indicating in-plane X and Y displacement directions, c) simulated translational displacement of the rotation center along the X, Y, and Z axes as a function of actuation voltage (bottom X-axis) for both CW and CCW actuation. The corresponding angular displacement is provided on the top X-axis for reference.

The displacements observed along the X, Y, and Z axes represent the cross-axis sensitivities of the structure, corresponding to unintended translational motions occurring during rotational actuation. As shown in Fig. 6(c), the displacement in the Y direction remains minimal across the full actuation range, indicating strong lateral symmetry and effective suppression of motion along this axis. The X-direction displacement is slightly larger but remains confined to the nanometer scale, reflecting minor coupling between rotational and lateral motion. In contrast, the Z-direction displacement exhibits a higher magnitude, which is attributed to the out-of-plane compliance of the suspension beams under electrostatic loading. Despite this, the overall displacement remains below 300 nm, confirming that out-of-plane deformation is well controlled. These results demonstrate that the proposed symmetric U-shaped suspension design effectively minimizes cross-axis sensitivities and maintains a stable center of rotation, which is critical for alignment-sensitive applications such as optical switching.

To evaluate how the unwanted lateral and out-of-plane motions of the rotary MEMS platform affect the optical coupling, we performed 3D finite-difference time-domain (FDTD) simulations using ANSYS Lumerical between two supposed waveguides that would lie above the structures. As the platform rotates, it experiences small shifts in X, Y, and Z directions. These small displacements, taken from the mechanical simulations, were applied directly in the optical model. Simulations were carried out at 0, 40, 80, and 150 V.

The movable and fixed SiN waveguides were modeled with a 435 nm × 200 nm inverted taper to match the fabrication constraints. A 2 µm air gap was considered between the fixed and movable waveguides, as this separation is imposed by the fabrication process after the gap is closed. For each voltage step, the corresponding mechanical displacement was modeled, and the TE-polarized fundamental mode was used as an input in the fixed input waveguide. Since the device is designed to operate in the C and L bands, the analysis was limited to 1530–1625 nm.

The coupling-efficiency curves in Fig. 7(a) show stable optical performance for all actuation voltages. The average normalized coupling efficiency in the C and L band changes only slightly, with values of 0.7821, 0.7779, 0.7755, and 0.7718 for 0, 40, 80, and 150 V, respectively. These minor variations reflect the small unwanted motion of the platform, which remains below 50 nm laterally and 300 nm vertically.

Fig. 7(b) and (c) show the simulated electric field in the Y-Z plane for 0 V and 150 V. This cross-section emphasizes the effect of vertical misalignment, which is larger than the lateral shift. At 150 V, the mode shape changes slightly, but no noticeable spreading or radiation is observed. This confirms that the pivot-stable architecture sufficiently limits vertical motion and preserves proper optical alignment.

Overall, the FDTD simulations show that the rotary MEMS actuator minimizes optical efficiency variations across the angular displacement range. Even at the maximum applied voltage, the change in coupling efficiency remains below 1%.

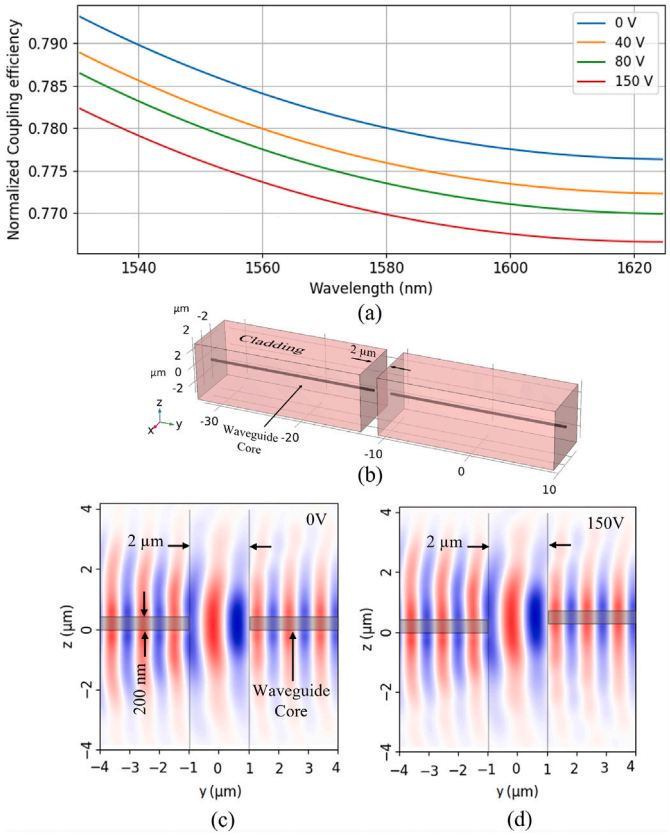


Fig. 7. (a) coupling efficiency from 3D FDTD simulations for actuation voltages ranging from 0 V to 150 V, (b) 3D representation of the simulated waveguide geometry, (c) side view of the simulated optical electric-field distribution at 0 V, indicating the effective 2 µm air gap and the 200 nm-thick SiN waveguide core, and (d) side view of the simulated optical electric-field distribution at 150 V, showing negligible deformation of the optical mode under voltage-induced Z-axis motion.

3.2. Measurements

To experimentally measure the angular displacement, gap-closing displacement, and undesired motion of the center of rotation during

actuation, microscope images were captured at actuation voltages ranging from 0 V to 150 V. A power supply (Keithley 22260B-800-1) was connected to the actuation electrodes (V_{in1} or V_{in2}), and the voltage was incremented in 10 V steps. At each step, high-resolution images were taken using an optical microscope (Keyence VHX-7000) to precisely track the motion of the center of rotation.

A MATLAB script was developed to analyze the microscope images and measure how much the micro-structure moved during actuation (see supplemental material). The images, captured at a high resolution of 2880 × 2160 pixels, were obtained across a voltage sweep from 0 V to 150 V in 10 V increments. Spatial calibration was established using a 10 μm reference scale bar that spanned 200 pixels, yielding a calibrated physical pixel size of 50 nm. It is notable, that this 50 nm value is the digital pixel size, meaning one pixel on the camera sensor covers 50 nm of physical space. It does not mean the microscope lenses can physically resolve details that small, as the actual optical resolution is still restricted by the standard diffraction limit of light.

To isolate structural contrast and reduce computational overhead, all RGB images were first converted to 8-bit grayscale matrices. Moreover, a digital smoothing algorithm was applied to the images. Subsequently, an edge-sharpening filter was utilized to enhance structural contrast and precisely define the physical boundaries of the moving components [39,52]. To detect movement, an absolute difference image was computed by subtracting the baseline resting state (0 V) from each actuated state using pixel-by-pixel subtraction. A specific region of interest (ROI) was defined using fixed spatial coordinates to isolate the target edge of the moving structure. Within this ROI, the algorithm identified the absolute maximum pixel intensity, which corresponds to the area of highest contrast shift (i.e., maximum physical displacement). To determine the spatial extent of this movement, the algorithm then quantified the total number of occurrences of this maximum intensity value, effectively calculating the length of the displaced leading edge in pixels. This pixel count was then directly converted into absolute physical dimensions using the 50 nm/pixel conversion factor.

Fig. 8(a) illustrates the output of this script, where the red-highlighted regions represent the displacement between the 0 V and 150 V states during CW rotation. In this case, the red region corresponds to the initial position of the MEMS structure at 0 V, while the gray region indicates the displaced position at 150 V actuation. Fig. 8(b) shows the output of the processed images for CCW motion. In this case, the gray region corresponds to the initial position at 0 V, while the red region indicates the displaced position at 150 V actuation. The color inversion between Fig. 8(a) and (b) reflects the opposite directions of motion during CW and CCW actuation, respectively.

To evaluate out-of-plane (i.e., Z-axis) displacement, a confocal laser microscope (LEXT-Olympus OLS4100) was used. Using these methods, these displacements were extracted to evaluate undesired translational motions during the in-plane rotation.

Fig. 9 shows the displacements of the pivot point along the X, Y, and Z directions as a function of actuation voltage during both CW and CCW rotations. All measurements were repeated five times in each rotation direction, and the averaged results are reported. The error bars in each plot represent the standard deviation (STD) across the five measurements, reflecting the repeatability and variability of the observed motions.

Fig. 9(a) shows the in-plane X and Y displacements during rotation. Under CW actuation, the two axes exhibit distinct movement patterns. The X displacement rises to approximately 50 nm at 10 V, undergoes a secondary shift to 100 nm at 70 V, and ultimately peaks at 170 nm at 150 V. Meanwhile, the Y displacement also shows an initial jump to 50 nm at 10 V, but then steadily climbs to reach 140 nm by 150 V.

For CCW actuation, a stepwise trend is observed alongside improved lateral stability in the Y direction. After an early spike to a magnitude of 100 nm at 10 V, this Y displacement remains highly stable up to 130 V before a minor shift to 120 nm at 150 V, indicating a more uniform

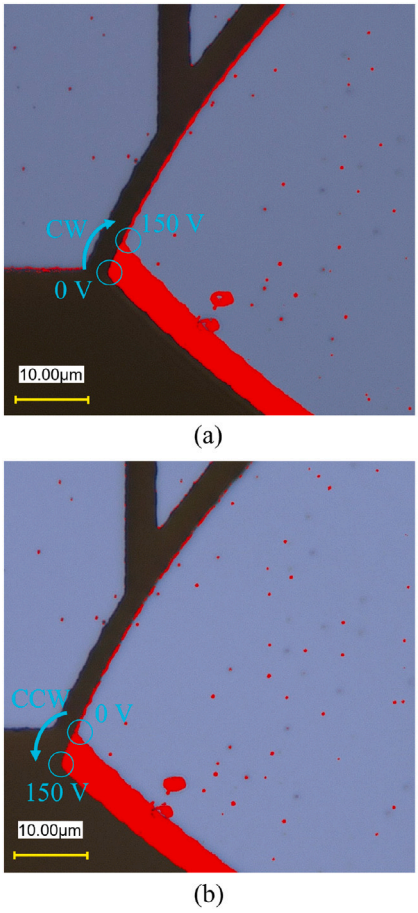


Fig. 8. Processed image output showing the pixel differences between the 0 V and 150 V actuation states. a) CW motion, where the red region corresponds to the initial position at 0 V and the gray region corresponds to the displaced position at 150 V, b) CCW motion, where the gray region corresponds to the initial position at 0 V and the red region corresponds to the displaced position at 150 V. The color inversion reflects the opposite direction of motion (For interpretation of the references to color in this figure legend, the reader is referred to the web version of this article.)

electrostatic force distribution. Conversely, the X displacement during CCW operation advances to 70 nm at 50 V and continues to grow, finalizing at 190 nm at the maximum 150 V.

As observed in the error bars of Fig. 9(a), the standard deviation is zero at certain actuation voltages, indicating that the extracted displacement was identical across all repeated measurements. Conversely, at other voltages, the error bars are larger. This variability is a direct consequence of the 50 nm/pixel calibrated digital sampling pitch. Because the displacement is extracted discretely based on pixel counts, a variation of even a single pixel in the algorithm's output between repeated measurements translates to a 50 nm shift in the calculated physical displacement. This digital discretization step leads to larger standard deviation values when minor measurement variations occur at the pixel boundaries.

Fig. 9(b) plots the out-of-plane Z displacement. A gradual increase is observed in both CW and CCW directions, from 50 nm at 0 V to approximately 300 nm at 150 V. The displacement trend is non-monotonic, featuring some inflection points, which suggest complex structural interactions such as tilting, vertical compliance, and possible electro-mechanical softening under high voltage. The near-symmetric Z-axis behavior between CW and CCW confirms that vertical deformation is dominated by global structural compliance rather than directional asymmetry.

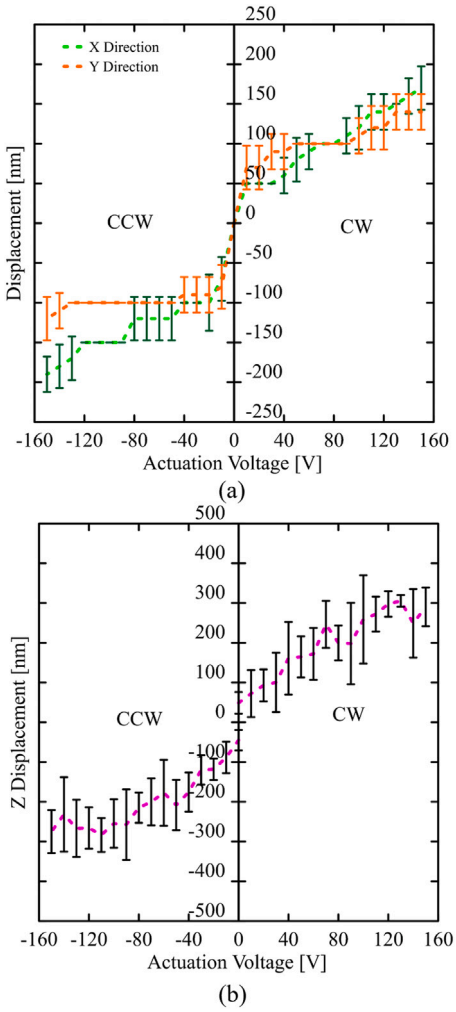


Fig. 9. Measured translational displacement of the center of rotation as a function of actuation voltage during both CW and CCW operation: a) in-plane X and Y displacements, and b) out-of-plane Z displacement. Error bars represent the standard deviation (STD) across five repeated measurements.

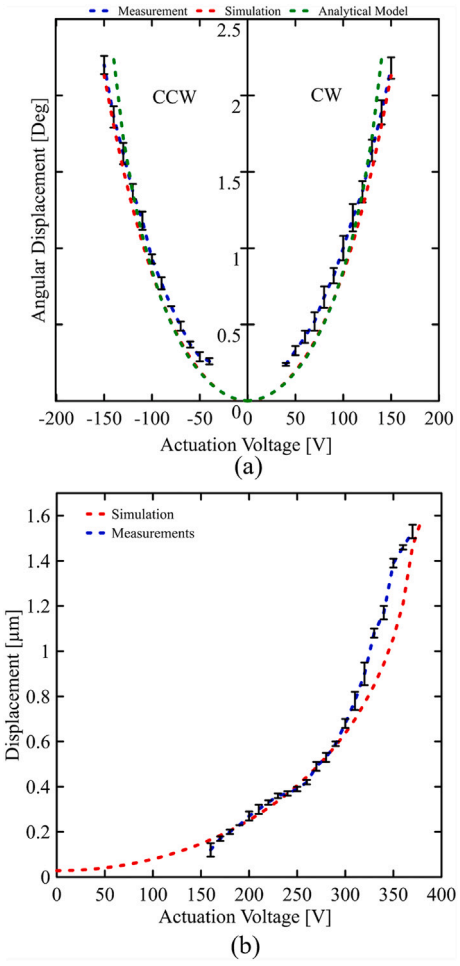


Fig. 10. Measured displacements of the fabricated MEMS structure: a) angular displacement, and b) lateral gap-closing displacement.

Rotational and gap-closing displacements were measured at each 10 V step of applied voltage with a Keithley 22260B-800-1 power supply until pull-in was reached. Fig. 10(a) illustrates the angular displacement as a function of actuation voltage. The FEM simulation results are represented by the red dashed line, the analytical model previously discussed is represented by the green dashed line, and the experimental measurements by the blue dashed line. Each measurement point is the average of five repeated measurements to ensure accuracy, and the STD is represented by the error bars. Numerical simulation results (red dashed line) show that a 150 V actuation voltage is sufficient to make the structure undergo a 2.2° rotation CW and CCW. The experimental results (blue dashed line) align with the simulation results, and achieved a 2.2° angular displacement at the same voltage for both directions. A quantitative comparison indicates that the analytical model overestimates the angular displacement relative to both FEM simulations and experimental measurements. For instance, at 130 V, the analytical model predicts an angular displacement of 2.4°, whereas the experimental measurement yields approximately 1.5°. At the maximum actuation voltage of 150 V, the analytical model predicts approximately 2.4°, whereas both simulation and experimental results reach about 2.2°, corresponding to an overestimation of approximately 9%. Because neglecting fringing fields in the analytical formulation inherently underestimates the electrostatic torque, the observed overestimation in displacement is primarily attributed to the idealized mechanical boundary conditions. Specifically, the physically fabricated structure exhibits slightly higher stiffness due to factors such as sidewall angling introduced during the DRIE etching and non-ideal rigid anchoring, which are not captured in the closed-form model. Despite these differences, the analytical model accurately captures the overall trend and provides a reliable first-order estimation of the device behavior.

It is notable that angular displacement measurements start at 40 V (and as discussed later, lateral gap-closing measurements begin at 160 V). At actuation voltages below these respective thresholds, the physical displacements induced by the structure are smaller than the digital pixel mapping limits achieved at the selected ×2000 magnification, causing them to fall within the measurement noise floor. Consequently, reliable displacement extraction in these low-voltage regimes is not feasible using the current optical setup. However, this limitation is strictly inherent to the optical metrology technique and does not negatively impact the overall characterization of the device. Within its primary operational range at higher voltages, the displacements become clearly distinguishable from the noise floor, and the extracted measurements align closely with the FEM simulation predictions.

Fig. 10(b) presents the measured lateral gap-closing displacement of the suspended platform, along with the corresponding actuation voltage required to close the gap between the platform and the gap-closing electrode (V_{GC}). The platform makes full contact with the stoppers at an actuation voltage of 380 V. Lateral displacement measurements were performed five times and averaged, consistent with the angular

Table 3
Performance comparison of electrostatically actuated in-plane rotary MEMS structures.

Reference	Angular displacement (°)	Actuation voltage (V)	Rotation sensitivity (° V^{-1})	Size (mm^2)	Unwanted displacement (nm)	Note
[46]	±9	60	0.15	1×1	Not reported	Serpentine springs used to achieve large in-plane rotation.
[2]	±1.5	190	0.007	2×1	Not reported	Virtual pivot linkage keeps a fixed rotation center for tunable laser alignment.
[2]	3	130	0.02	2×1	Not reported	Long-arm rotary actuator with external mirror and stable pivot.
[7]	±9.5	180	0.53	1.3×1.0	Not reported	Circular comb-drive with latching for optical switching.
[7]	±5	350	0.014	1.3×1.0	Not reported	Circular comb-drive on ⟨110⟩ silicon wafer.
[50]	±2.4	50	0.048	0.6×1.3	Not reported	Circular comb-drive using a double-clamped beam for real pivot point.
[50]	±4.7	70	0.067	0.6×1.3	Not reported	Circular comb-drive using a cantilever beam for virtual pivot.
[14]	±2.9	234	0.012	1×1.3	Not reported	Circular-shaped springs with rotary combs.
[32]	±4.5	70	0.064	24×24	Not reported	Contactless rotary MEMS using EBG-based waveguide switching; avoids stiction via non-contact operation.
[33]	±2.25	60	0.037	Not reported	Not reported	Vertical comb-drive micromirror with torsion beams; stability limited by lateral and rotational pull-in effects.
This Work	±2.2	150	0.015	1×2	X/Y < 190, Z < 300	U-shaped spring minimizes lateral and out-of-plane motion; includes gap-closing mechanism.

displacement measurements. Displacement became optically observable under the microscope at approximately 160 V. Again, the experimental and simulation results exhibit good agreement.

4. Discussion

Table 3 provides an overview of electrostatic rotary MEMS designs published in the literature. Angular displacement, actuation voltages, rotation sensitivity, and device footprint are compared.

In-plane rotary MEMS actuators have been demonstrated in a wide range of applications, including optical beam steering, tunable lasers, etc. However, they often require high actuation voltages. Several studies have reported different rotary MEMS structures based on electrostatic actuation. For example, Yeh et al. [46] demonstrated a rotary comb-drive actuator using serpentine spring suspensions that achieved angular deflections of approximately ±9° at an actuation voltage below 60 V. While the serpentine flexures allowed large rotations at relatively low voltages, a trade-off of this flexure design was the lateral shift of the rotation center. According to their research, basic flexure designs such as serpentine or straight beams can cause the center of the rotor to move unintentionally during actuation, which may degrade rotational accuracy in precision applications.

Amin et al. [2] developed a “virtual pivot” rotary comb actuator that uses a symmetric linkage of rotating arms to emulate a pin joint at a point in space. This enabled a small angular range (±1.5° at 190 V). In a related design, the same group extended the rotating arms beyond 5 mm and mounted an external mirror, achieving about 3° rotation at 130 V. Although the long-arm actuator was large (area 2 × 1 mm^2), it provided a mechanically stable pivot for the mirror with negligible lateral shift during motion. However, the structures exhibited an undesirable amount of lateral translational motion. In another work, Zhang et al. [50] proposed a double-clamped beam achieving 4.7° rotation at 70 V, though at the expense of a large device footprint.

Despite the wide range of actuator topologies and design optimizations discussed, it is noteworthy that none of the listed studies reported direct experimental measurements or simulation based quantification of the undesired lateral translational motion of the rotation center during actuation. While many designs rely on structural symmetry or virtual pivots to provide minimal lateral shift, this important aspect of dynamic performance has remained unverified by measurement across the literature, to the best of the authors’ knowledge. In contrast, this work addresses this gap by explicitly measuring the translational displacement during rotational actuation, thus quantitatively reporting on in-plane rotational fidelity.

Measurements indicate that the lateral unwanted translational motion is less than 42 nm in-plane and less than 300 nm out-of-plane. The measured unwanted translational displacements along the X, Y, and Z directions do not exactly match the FEM predictions, which is expected given differences between the modeling assumptions and the experimental conditions. In the simulations, the structure is assumed to be perfectly symmetric with ideal material properties, uniform electrostatic loading, and simplified boundary conditions, whereas the fabricated device can have fabrication variations, slight geometric asymmetries, and residual stress that can impact stiffness resulting in the simulation and experimental results discrepancies. Experimentally, the in-plane X and Y displacements were extracted from optical microscope images using a MATLAB pixel-difference method, where nanometer-scale motion was measured from the number of pixels. In contrast, the out-of-plane Z displacement was measured using a confocal laser microscope, which directly measures surface height rather than lateral position. As a result, the same pixel-based image processing approach used for X and Y could not be applied to the Z direction, leading to different measurement resolutions between in-plane and out-of-plane data. Despite these discrepancies, both simulation and experiment consistently confirm that the unwanted in-plane and out-of-plane motions remain confined to the nanometer range, demonstrating that the proposed structure maintains a stable pivot point during rotational actuation.

The relatively high actuation voltage required for the proposed device is primarily due to the electrostatic actuation mechanism and the relatively large gap between the comb-drive electrodes. While this voltage level is typical for electrostatic rotary MEMS actuators, it may limit direct integration in low-voltage applications. Potential strategies to reduce the actuation voltage include decreasing the gap between comb fingers, increasing the number of fingers to enhance the electrostatic force, or reducing the stiffness of the suspension springs. However, these approaches introduce trade-offs. For example, reducing

the gap increases the risk of pull-in instability and fabrication challenges, whereas lowering the spring stiffness may degrade the stability of the rotation center and increase susceptibility to parasitic motion. Similarly, increasing the device size to enhance force generation may compromise footprint constraints. Therefore, the current design represents a balanced trade-off between actuation voltage, rotational stability and device size.

Beyond angular displacement and spatial footprint, the suitability of rotary MEMS actuators is also dictated by metrics such as energy efficiency, reliability, and mechanical bandwidth. In terms of energy efficiency, the proposed electrostatic actuator consumes near-zero static power—requiring energy primarily during the charging and discharging of the comb-drive capacitance—making it highly advantageous compared to electrothermal or electromagnetic actuators that require continuous current flow. Regarding reliability, the use of a flexure-based U-shaped suspension architecture entirely eliminates the physical rubbing and friction associated with traditional pin-joint rotary hubs, thereby mitigating mechanical wear and extending the operational lifespan of the pivot center. Finally, while mechanical bandwidth (resonance frequency) was not explicitly characterized in this study, it remains a critical trade-off factor; any future design iterations aimed at reducing the actuation voltage by lowering the suspension stiffness will inherently reduce the mechanical bandwidth, thereby limiting the maximum switching speed for optical applications.

Overall, the proposed actuator offers a balanced performance relative to prior electrostatic rotary MEMS designs. While it does not achieve the largest deflections reported, it maintains competitive sensitivity ($0.015\ ^\circ\ V^{-1}$) within a compact footprint and, most importantly, uniquely quantifies and suppresses lateral and out-of-plane unwanted drift during rotation.

5. Conclusion

This work introduces a pivot stable, electrostatically actuated rotary MEMS structure that delivers precise in plane angular motion while suppressing parasitic translation and out of plane deflection. The combination of U-shaped suspension springs with a circularly symmetric curved comb finger architecture enables inherently balanced bidirectional actuation and contributes to the high stability of the rotating platform.

The structure achieved a maximum angular displacement of ±2.2° at 150 V, and this result was corroborated through both finite element simulations and experimental characterization. The close agreement between measured and simulated responses indicated that the dominant mechanical behavior was well captured. Although the analytical model slightly overestimated the rotation, primarily due to idealizations such as neglecting fringing fields, fabrication induced residual stress, and geometric non idealities, it remains valuable for rapid early stage sizing and design trade studies.

A central contribution of this study was the explicit experimental quantification of parasitic motion during actuation, which is commonly assumed negligible and therefore is seldom reported. Measured lateral displacements remained below 190 nm, and out of plane motion was maintained under 300 nm, demonstrating that the structure preserved alignment integrity under drive and was well suited for applications with tight tolerance budgets. This behavior was also assessed using FDTD optical simulations with hypothetical waveguides assumed on the structure.

Overall, the device offers a compact footprint, low power electrostatic actuation, and minimal parasitic motion, making it a good candidate for integration into alignment critical MEMS platforms, including MOEMS switches and RF MEMS systems.

Future work is expected to focus on reducing the actuation voltage, improving rotational sensitivity, and integrating optical elements such as silicon nitride waveguides onto the central platform to realize fully functional low loss MOEMS switches. These developments are expected to enable compact scalable optical switching architectures relevant to next generation data center and telecommunication infrastructure.

CRediT authorship contribution statement

Navid Heidari: Writing – original draft, Visualization, Validation, Software, Methodology, Investigation, Formal analysis, Data curation, Conceptualization. **Julian L. Pita Ruiz:** Software, Formal analysis. **Mathieu Gratuze:** Writing – review & editing, Investigation. **Seyedfakhreddin Nabavi:** Writing – review & editing, Software. **Michaël Ménard:** Writing – review & editing, Supervision. **Frederic Nabki:** Writing – review & editing, Supervision.

Declaration of competing interest

The authors declare that they have no known competing financial interests or personal relationships that could have appeared to influence the work reported in this paper.

Acknowledgements

The authors would like to express their thanks to CMC Microsystems for providing the necessary computer-aided design (CAD) and finite element analysis (FEA) tools, as well as access to the micro-fabrication process. The authors would also like to thank the LaCIME for the use of their research labs.

Appendix A. Supplementary data

Supplementary data for this article can be found online at doi:10.1016/j.sna.2026.118047.

Data availability

Data will be made available on request.

References

[1] M. Ahmad, M. Bahri, M. Sawan, MEMS micromirror actuation techniques: a comprehensive review of trends, innovations, and future prospects, Micromachines 15 (2024) 1233. https://doi.org/10.3390/mi15101233, https://www.mdpi.com/2072-666X/15/10/1233.

[2] T. Amin, M. Huda, Y. Ning, G. McKinnon, J. Tulip, W. Jäger, A virtual pivot point MEMS rotary comb actuator for tunable laser applications, in: Laser Beam Shaping XIII, SPIE, 2012, pp. 105–113.

[3] T.M.F. Amin, M.Q. Huda, J. Tulip, W. Jager, Design and fabrication of a long-arm comb-drive rotary actuator with externally mounted mirror for optical applications, J. Microelectromechanical Syst. 24 (2015) 1565–1574. https://doi.org/10.1109/JMEMS.2015.2423285, http://ieeexplore.ieee.org/document/7103014/.

[4] S.S. Ba Hashwan, M.H.M. Khir, I.M. Nawi, M.R. Ahmad, M. Hanif, F. Zahoor, Y. Al-Douri, A.S. Algamili, U.I. Bature, S.S. Alabsi, M.O.B. Sabbea, M. Junaid, A review of piezoelectric MEMS sensors and actuators for gas detection application, Discov. Nano 18 (2023) 25, https://doi.org/10.1186/s11671-023-03779-8

[5] U. Baran, W.O. Davis, S. Holmstrom, D. Brown, J. Sharma, S.K. Gokce, H. Urey, Linear-stiffness rotary MEMS stage, J. Microelectromechanical Syst. 21 (2012) 514–516. https://doi.org/10.1109/jmems.2011.2182504, http://ieeexplore.ieee.org/document/6145591/.

[6] G. Bhatt, K. Manoharan, P.S. Chauhan, S. Bhattacharya, MEMS sensors for automotive applications: a review, Sens. Automot. Aerosp. Appl. (2019) 223–239.

[7] J. Briere, M.Y. Elsayed, M. Saidani, M. Bérard, P.O. Beaulieu, H. Rabbani-Haghighi, F. Nabki, M. Ménard, Rotating circular micro-platform with integrated waveguides and latching arm for reconfigurable integrated optics, Micromachines 8 (2017) 354.

[8] Y. Cao, J. Dong, Self-sensing and control of soft electrothermal actuator, in: IEEE/ASME Transactions on Mechatronics, vol. 26, 2021, pp. 854–863. https://doi.org/10.1109/TMECH.2020.3009237, https://ieeexplore.ieee.org/document/9140392/.

[9] H. Chang, H. Zhao, F. Ye, G. Yuan, J. Xie, M. Kraft, W. Yuan, A rotary comb-actuated microgripper with a large displacement range, Microsyst. Technol. 20 (2014) 119–126. https://doi.org/10.1007/s00542-013-1737-8, http://link.springer.com/10.1007/s00542-013-1737-8.

[10] A. Cowen, G. Hames, K. Glukh, B. Hardy, PiezoMUMPST™ Design Handbook, Rev. 1.3, MEMSCAP Inc., 2014, pp. 1–28, http://www.memscap.com.

[11] X. Gao, J. Yang, J. Wu, X. Xin, Z. Li, X. Yuan, X. Shen, S. Dong, Piezoelectric actuators and motors: materials, designs, and applications, Adv. Mater. Technol. 5 (2020) 1900716. https://doi.org/10.1002/admt.201900716, https://onlinelibrary.wiley.com/doi/10.1002/admt.201900716.

[12] K.L. Genter, P. Kabos, V.M. Bright, Electrostatic comb drive actuator array with integrated cantilever for scanning probe applications, in: 2021 21st International Conference on Solid-State Sensors, Actuators and Microsystems (Transducers), IEEE, Orlando, FL, USA, 2021, pp. 619–622. https://doi.org/10.1109/Transducers50396.2021.9495474, https://ieeexplore.ieee.org/document/9495474/.

[13] W.A. Gill, I. Howard, I. Mazhar, K. McKee, A review of MEMS vibrating gyroscopes and their reliability issues in harsh environments, Sensors 22 (2022) 7405. https://doi.org/10.3390/s22197405, https://www.mdpi.com/1424-8220/22/19/7405.

[14] N. Heidari, J.L. Pita Ruiz, S. Nabavi, M. Ménard, F. Nabki, Reconfigurable electrostatically actuated 1 × 5 rotary MOEMS switch, Opt. Express 33 (2025) 10726. https://doi.org/10.1364/OE.545403, https://opg.optica.org/abstract.cfm?URI=oe-33-5-10726.

[15] M. Hommel, H. Knab, S.G. Yousef, Reliability of automotive and consumer MEMS sensors - an overview, Microelectron. Reliab. 126 (2021) 114252. https://doi.org/10.1016/j.microrel.2021.114252, https://www.sciencedirect.com/science/article/pii/S0026271421002183.

[16] Y. Honjol, V.S. Rajkumar, C. Parent-Harvey, K. Selvasandran, S. Kordlouie, M. Comeau-Gauthier, E. Harvey, G. Merle, Current view and prospect: implantable pressure sensors for health and surgical care, Med. Devices Sens. 3 (2020) e10068. https://doi.org/10.1002/mds3.10068, https://onlinelibrary.wiley.com/doi/10.1002/mds3.10068.

[17] M. Huda, T. Amin, Y. Ning, G. McKinnon, J. Tulip, W. Jäger, Rotary MEMS comb-drive actuator with large deflection for photonic applications, in: Micromachining and Microfabrication Process Technology XVII, SPIE, 2012, pp. 30–37.

[18] H. Hussein, H. Fariborzi, M.I. Younis, Modeling of beam electrothermal actuators, J. Microelectromechanical Syst. 29 (2020) 1570–1581. https://doi.org/10.1109/JMEMS.2020.3033477, https://ieeexplore.ieee.org/document/9245585/.

[19] S. Janson, H. Helvajian, K. Breuer, MEMS, microengineering and aerospace systems, in: 30th Fluid Dynamics Conference, American Institute of Aeronautics and Astronautics, Norfolk, VA, U.S.A. URL, 1999, https://doi.org/10.2514/6.1999-3802, https://arc.aiaa.org/doi/10.2514/6.1999-3802.

[20] L. Jin, Applications and prospects of MEMS sensors in automotive, J. Phys.: Conf. Series 1884, 012010. (2021), https://doi.org/10.1088/1742-6596/1884/1/012010, https://dx.doi.org/10.1088/1742-6596/1884/1/012010.

[21] J.W. Judy, Microelectromechanical systems (MEMS): fabrication, design and applications, Smart Mater. Struct. 10 (2001) 1115, https://doi.org/10.1088/0964-1726/10/6/301, https://dx.doi.org/10.1088/0964-1726/10/6/301.

[22] V. Kaajakari, Practical MEMS, Small Gear Publishing, ISBN-10 = 0982299109, 2009.

[23] A. Kashani Ilkhechi, H. Mirzajani, E. Najafi Aghdam, H. Badri Ghavifekr, A new electrostatically actuated rotary three-state DC-contact RF MEMS switch for antenna switch applications, Microsyst. Technol. 23 (2017) 231–243.

[24] M.S. Khan, M.O. Tariq, M. Nawaz, J. Ahmed, MEMS sensors for diagnostics and treatment in the fight against COVID-19 and other pandemics, IEEE Access 9 (2021) 61123–61149. https://doi.org/10.1109/ACCESS.2021.3073958, https://ieeexplore.ieee.org/document/9406575/.

[25] Y. Li, P. Denny, C.M. Ho, C. Montemagno, W. Shi, F. Qi, B. Wu, L. Wolinsky, D. Wong, The oral fluid MEMS/NEMS chip (OFMNC): diagnostic & translational applications, Adv. Dent. Res. 18 (2005) 3–5. https://doi.org/10.1177/154407370501800102, https://journals.sagepub.com/doi/10.1177/154407370501800102.

[26] S. Lyu, Y. Tamaki, K. Morishita, K. Saito, Development of rotary-type electrostatic motor for MEMS microrobot, Artif. Life Robot. 30 (2025) 148–155. https://doi.org/10.1007/s10015-024-00996-x, https://link.springer.com/10.1007/s10015-024-00996-x.

[27] S. Nabavi, M. Ménard, F. Nabki, A SOI out-of-plane electrostatic MEMS actuator based on in-plane motion, J. Microelectromechanical Syst. 31 (2022) 820–829, https://doi.org/10.1109/JMEMS.2022.3190829

[28] B. Piriyanont, A.G. Fowler, S.O. Reza Moheimani, Force-controlled MEMS rotary microgripper, J. Microelectromechanical Syst. 24 (2015) 1164–1172. https://doi.org/10.1109/JMEMS.2015.2388539, http://ieeexplore.ieee.org/document/7018056/.

[29] C. Qi, D. Han, T. Shinshi, A MEMS-based electromagnetic membrane actuator utilizing bonded magnets with large displacement, Sens. Actuators a Phys. 330 (2021) 112834. https://doi.org/10.1016/j.sna.2021.112834, https://www.sciencedirect.com/science/article/pii/S0924424721002971.

[30] Z. Qiu, W. Piyawattanamatha, New endoscopic imaging technology based on MEMS sensors and actuators, Micromachines 8 (2017) 210. https://doi.org/10.3390/mi8070210, https://www.mdpi.com/2072-666X/8/7/210.

[31] A.N. Radwan, R.S. Almikhlafi, M.S.M. Soliman, Performance comparison of commonly used MEMS Springs: double-folded, U-shaped and fish-Hook, in: 2013 Saudi International Electronics, Communications and Photonics Conference, IEEE, Fira, 2013, pp. 1–6. https://doi.org/10.1109/siecpc.2013.6550993, http://ieeexplore.ieee.org/document/6550993/.

[32] S. Rahiminejad, S. van Berkel, R. Lin, S. Khanal, C. Jung-Kubiak, G. Chattopadhyay, M. Rais-Zadeh, 500-750 GHz contactless rotating MEMS single-pole double-throw waveguide switch, J. Microelectromech. Syst. 33 (5) (2024) 532–542.

[33] Y. Shan, L. Qian, J. Wang, K. Wang, P. Zhou, W. Li, W. Shen, Driving principle and stability analysis of vertical comb-drive actuator for scanning micromirrors. Micromachines 15, 226. URL: 2024, https://doi.org/10.3390/mi15020226: https://www.mdpi.com/2072-666X/15/2/226.

[34] S. Sharma, S. Nabavi, A.A.S. Rabih, M. Ménard, F. Nabki, Hybrid MEMS actuator with 3 degrees-of- freedom for efficient planar optical switching, J. Microelectromechanical Syst. 32 (2023) 593–603, https://doi.org/10.1109/JMEMS.2023.3322223

[35] P. Song, Z. Ma, J. Ma, L. Yang, J. Wei, Y. Zhao, M. Zhang, F. Yang, X. Wang, Recent progress of miniature MEMS pressure sensors. Micromachines 11, 56. URL: 2020, https://doi.org/10.3390/mi11010056. https://www.mdpi.com/2072-666X/11/1/56.

[36] K. Srinivasa Rao, M. Hamza, P. Ashok Kumar, K. Girija Sravani, Design and optimization of MEMS based piezoelectric actuator for drug delivery systems, Microsyst. Technol. 26 (2020) 1671–1679, https://doi.org/10.1007/s00542-019-04712-9

[37] S. Suman, D. Punetha, S.K. Pandey, Improvement in sensing characteristics of silicon microstructure based MEMS capacitive sensor for automotive applications, Silicon 13 (2021) 1475–1483, https://doi.org/10.1007/s12633-020-00540-z

[38] M. Tanaka, An industrial and applied review of new MEMS devices features, Microelectron. Eng. 84 (2007) 1341–1344. https://doi.org/10.1016/j.mee.2007.01.232, https://linkinghub.elsevier.com/retrieve/pii/S0167931707001633.

[39] The MathWorks Inc, Find Edges in 2-D Grayscale Image - MATLAB Edge, The MathWorks Inc, Natick, MA. 2026, https://www.mathworks.com/help/images/ref/edge.html.

[40] P.H. Tran, D.S. Mukai, M. Brenner, Z. Chen, In vivo endoscopic optical coherence tomography by use of a rotational microelectromechanical system probe, Opt. Lett. 29 (2004) 1236. https://doi.org/10.1364/OL.29.001236, https://opg.optica.org/abstract.cfm?URI=ol-29-11-1236.

[41] C.C. Tu, K. Fanchiang, C.H. Liu, 1xN rotary vertical micromirror for optical switching applications, in: MOEMS and Miniaturized Systems V, SPIE, 2005, pp. 14–22.

[42] C.C. Tu, K. Fanchiang, C.H. Liu, 1 ×N rotary vertical micromirror for optical switching applications, 2005, 14. https://doi.org/10.1117/12.589810, San Jose, CA: http://proceedings.spiedigitallibrary.org/proceeding.aspx?doi=10.1117/12.589810.

[43] O. Ulkir, Design and fabrication of an electrothermal MEMS micro-actuator with 3D printing technology, Mater. Res. Express 7 (2020) 075015. https://doi.org/10.1088/2053-1591/aba8e3, https://dx.doi.org/10.1088/2053-1591/aba8e3.

[44] R. Urata, H. Liu, K. Yasumura, E. Mao, J. Berger, X. Zhou, C. Lam, R. Bannon, D. Hutchinson, D. Nelson, L. Poutievski, A. Singh, J. Ong, A. Vahdat, Apollo: large-scale deployment of optical circuit switching for datacenter networking, 2023, https://doi.org/10.1364/OFC.2023.M2G.1

[45] T.A.S. Weis, B.V. Lahijani, K. Tsoukalas, M. Albrechtsen, S. Stobbe, Design, fabrication, and characterization of electrostatic comb-drive actuators for nano-electromechanical silicon photonics. 2023, https://doi.org/10.48550/arXiv.2307.01122: http://arxiv.org/abs/2307.01122. arXiv:2307.01122 [physics].

[46] J.A. Yeh, C.N. Chen, Y.S. Lui, Large rotation actuated by in-plane rotary comb-drives with serpentine spring suspension, J. Micromech. Microeng. 15 (2004) 201.

[47] Z. You, L. Wei, M. Zhang, F. Yang, X. Wang, Hermetic and bioresorbable packaging materials for MEMS implantable pressure sensors: a review, IEEE Sens. J. 22 (2022) 23633–23648. https://doi.org/10.1109/JSEN.2022.3214337, https://ieeexplore.ieee.org/document/9925144/.

[48] J. Yunas, B. Mulyanti, I. Hamidah, M. Mohd Said, R.E. Pawinanto, W.A.F. Wan Ali, A. Subandi, A.A. Hamzah, R. Latif, B. Yeop Majlis, Polymer-based MEMS electromagnetic actuator for biomedical application: a review, Polymers 12 (2020) 1184. https://doi.org/10.3390/polym12051184, https://www.mdpi.com/2073-4360/12/5/1184.

[49] R. Zhang, J. Qu, Y. Cao, X. Zhang, Y. Jia, X. Wang, W. Zhou, H. Xie, An integrated capacitive sensing method for electrostatic comb-drive micromirrors, Sens. Actuators a Phys. 357 (2023) 114416. https://doi.org/10.1016/j.sna.2023.114416, https://www.sciencedirect.com/science/article/pii/S0924424723002650.

[50] X. Zhang, A. Liu, C. Lu, D. Tang, A real pivot structure for MEMS tunable lasers, J. Microelectromechanical Syst. 16 (2007) 269–278.

[51] G. Zhanshe, C. Fucheng, L. Boyu, C. Le, L. Chao, S. Ke, Research development of silicon MEMS gyroscopes: a review, Microsyst. Technol. 21 (2015) 2053–2066. https://doi.org/10.1007/s00542-015-2645-x, http://link.springer.com/10.1007/s00542-015-2645-x.

[52] Y. Zheng, S. Li, Y. Xiang, Z. Zhu, Crack defect detection processing algorithm and method of MEMS devices based on image processing technology, IEEE Access 11 (2023) 126323–126334. https://doi.org/10.1109/ACCESS.2023.3331152, https://ieeexplore.ieee.org/document/10311554/.

[53] Y. Zhu, J. Pal, Low-voltage and high-reliability RF MEMS switch with combined electrothermal and electrostatic actuation, Micromachines 12 (2021) 1237. https://doi.org/10.3390/mi12101237, https://www.mdpi.com/2072-666X/12/10/1237.

Author biography

Navid Heidari received the B.Sc. degree in Materials Engineering from the University of Maragheh, Iran, in 2013, and the M.Sc. degree in Nanotechnology Engineering from Sapienza University of Rome, Italy, in 2020. He received the Ph.D. degree in Electrical Engineering from the École de Technologie Supérieure (ÉTS), Montreal, Canada, in 2026. His research focuses on the design and application of MEMS structures, particularly for use in optical technologies. His areas of interest include MEMS, sensors, and optical switches.

Julian L. Pita Ruiz received the B.Sc. degree in electronics engineering from the National University of Colombia in 2011, the M.Sc. degree in electrical engineering from São Paulo State University, Brazil, in 2014, and the Ph.D. degree in electrical engineering from the University of Campinas, Brazil, in 2018. He was a postdoctoral fellow with the Photonics Research Center (Photonicamp), Brazil, and with the Université du Québec á Montréal (UQÁM), Montréal, QC, Canada. He is currently an associate researcher with the Micro2 Laboratory at the École de Technologie Supérieure (ÉTS), Montréal, QC, Canada, working closely with the Laboratory of Micro and Nanofabrication (LMN), INRS, Varennes, QC, Canada. His research focuses on integrated photonics for optical communication systems and emerging technologies, including inverse design of photonic devices, fiber-to-chip interfaces, and nanofabrication for scalable, high-performance optical systems. Dr. Pita has authored and coauthored more than 50 publications and holds one issued patent and one pending patent application. He serves as an active reviewer for journals such as ACS Photonics, Optics Letters, Optics Express, and Optics Communications.

Mathieu Gratuze received a Master's degree with a major in electronics and microelectronics architecture from the École Supérieure de Chimie Physique Électronique de Lyon (CPE Lyon), Lyon, France, in 2017, and an M.Sc. degree in electrical and electronic engineering from École Centrale de Lyon (Centrale Lyon), France, in 2017. He received his Ph.D. in electrical engineering in 2022 from École de Technologie Supérieure, Montréal, QC, Canada. He is currently working as an associate researcher with the LaCIME (Laboratoire de Communications et d'Intégration de la Microélectronique), Department of Electrical Engineering, in the École de Technologie Supérieure, Montréal, QC, Canada. His research interests include design, modeling and characterization of piezoelectric MEMS transducers.

Seyedfakhreddin Nabavi was born in Hamedan, Iran, in 1991. He received the B.Sc. degree (Hons.) in biomedical engineering (bioelectric) from the Sahand University of Technology, Tabriz, Iran, in 2013, the M.Sc. degree in electrical and electronic engineering from Ozyegin University, Istanbul, Turkey, in 2015, and the Ph.D. degree from the Memorial University of Newfoundland, St. John's, NL, Canada, in April 2019. He was a Post-Doctoral Fellow with the Department of Electrical and Computer Engineering, McGill University, Montreal, QC, Canada. Currently, he is a Research Associate at the École de Technologie Supérieure, Montreal, a constituent of the University of Quebec. Dr. Nabavi has published over 38 publications and holds eight pending patent applications in the areas of sensors and wearable devices. His research interests include the design and modeling of MEMS transducers and actuators for industrial and biomedical applications and the design of analog circuits, such as sensor interfaces and power management systems. He was identified as a Top Reviewer of Applied Physics Letters (APL) in 2018. He has served as an invited reviewer for multiple scholarly journals and conferences, such as IEEE Transactions on Biomedical Engineering, and the IEEE SENSORS Conference.

Michaël Ménard was born in Québec City, QC, Canada. He received the B.Eng. and Ph.D. degrees in electrical engineering from McGill University, Montréal, QC, Canada, in 2002 and 2009, respectively. From 2009 to 2011, he was a Postdoctoral Fellow with the Cornell Nanophotonics Group under the supervision of Prof. Michal Lipson. In June 2011, he joined the Microelectronics Program at the Université du Québec á Montréal (UQAM), where he remained until September 2021, when he joined the Department of Electrical Engineering at the École de technologie supérieure (ÉTS), Montréal, QC, Canada. He co-manages the Microtechnology and Microsystems Laboratory. In 2019, he was a Visiting Researcher with the Department of Applied Physics at the State University of Campinas (UNICAMP), São Paulo, Brazil. He has authored or co-authored over 100 scientific publications and holds five issued patents and three pending patent applications. His research interests include integrated optics, silicon photonics, nonlinear optics, micro-opto-electro-mechanical systems (MOEMS), optomechanics, and microfabrication. Dr. Ménard is a member of the Ordre des ingénieurs du Québec. He currently holds or has previously held research funding from the Microsystems Strategic Alliance of Québec (ReSMiQ), the Centre for Optics, Photonics and Lasers (COPL), the Fonds de recherche du Québec – Nature et technologies (FRQNT), Prompt Québec, PRIMA Québec, and the Natural Sciences and Engineering Research Council of Canada (NSERC).

Frederic Nabki received the B.Eng. degree in electrical engineering with honors and the PhD degree in electrical engineering from McGill University, Montreal, QC, Canada, in 2003 and 2010, respectively. He began his academic career in 2008 as an Associate Professor in Microelectronics Engineering at the Université du Québec á Montréal (UQAM). In 2016, he joined the École de technologie supérieure (ÉTS), also in Montreal, QC, where he is currently a Professor in the Department of Electrical Engineering. His research interests include microelectromechanical systems (MEMS), RF and analog microelectronics, and heterogeneous integration. He has contributed extensively to the design and modeling of MEMS devices, CMOS/MEMS integration, the development of advanced MEMS fabrication processes, and the design of CMOS phase-locked loops, UWB transceivers, and sensor interface circuits. He has authored or co-authored over two hundred scientific publications, two book chapters, and holds 48 issued patents in these areas. Prof. Nabki is a member of the Communications and Microelectronic Integration Laboratory (LACIME) at ETS. He also jointly manages the Microtechnology and Microsystems Laboratory (Micro2). He served as the Secretary and Treasurer of the Montreal Section of the IEEE from 2013 to 2017, and was local arrangements chair of several international IEEE conferences held in Montreal: ISCAS 2016, NEWCAS 2012 & 2018 and Life Sciences Conference 2018. Moreover, he was a TPC member of the NEWCAS conference between 2013 and 2020 and TPC co-chair in 2022. He has been the recipient of the Governor General of Canada's Academic Bronze Medal, the UQAM Faculty of Science Early Career Research Award, the ETS Board of Directors Research Award and the IEEE Canada J.J. Archambault Merit Award. He holds or has held financial support from the Microsystems Strategic Alliance of Quebec (ReSMiQ), the Quebec Fund for Research in Nature and Technology (FRQNT), the Ministry of Economy, Science and Innovation (MESI) of Quebec, the Natural Sciences and Engineering Research Council of Canada (NSERC), and the Canada Foundation for Innovation (CFI).